Science Advances

8 NOVEMBER 2024

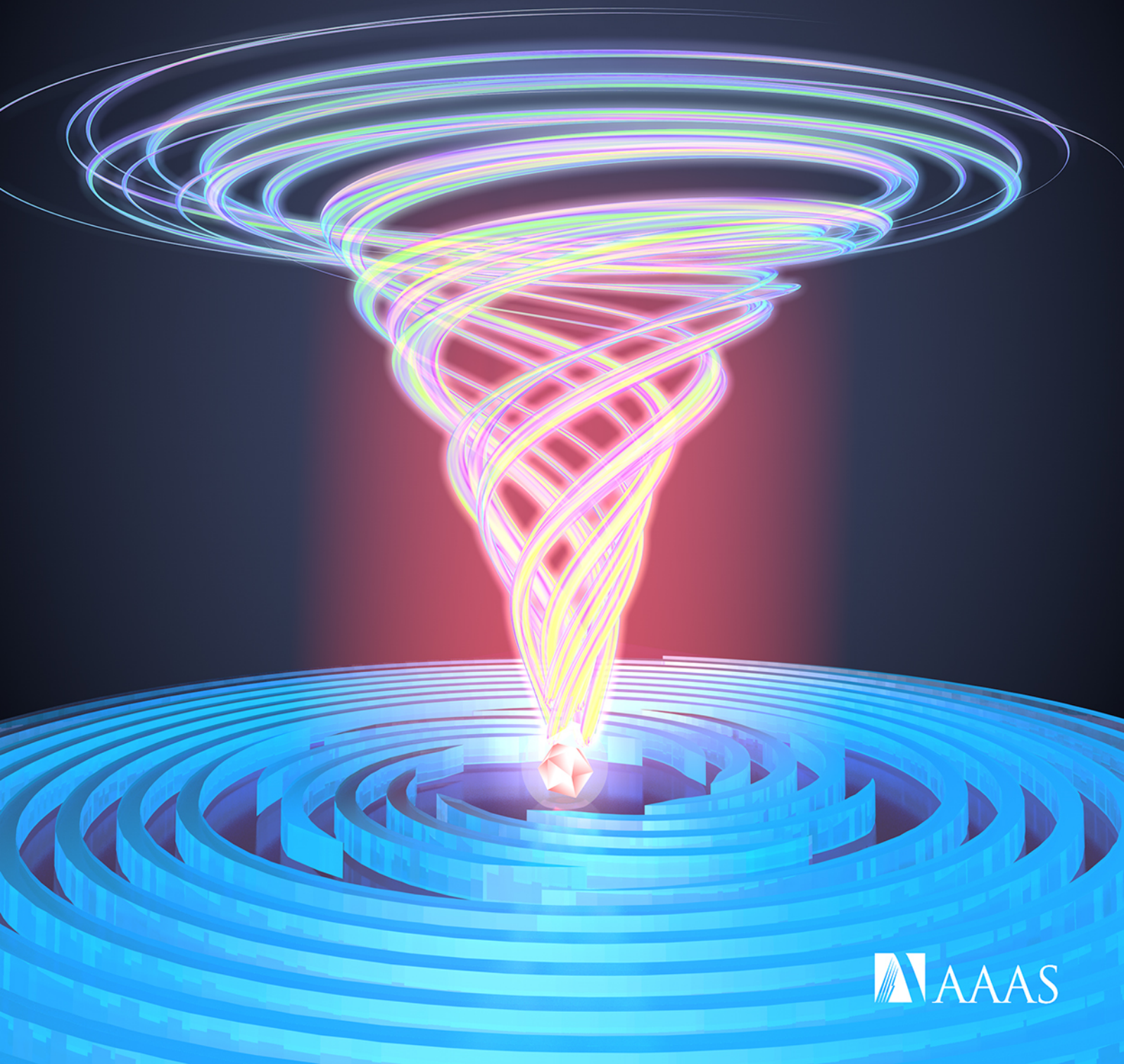

AAAS

OPTICS

High-dimensional spin-orbital single-photon sources

Yinhui Kan[1]*†, Xujing Liu[1]†, Shailesh Kumar[1], Liudmilla F. Kulikova[2], Valery A. Davydov[2], Viatcheslav N. Agafonov[3], Sergey I. Bozhevolnyi[1]*

Hybrid integration of solid-state quantum emitters (QEs) into nanophotonic structures opens enticing perspectives for exploiting multiple degrees of freedom of single-photon sources for on-chip quantum photonic applications. However, the state-of-the-art single-photon sources are mostly limited to two-level states or scalar vortex beams. Direct generation of high-dimensional structured single photons remains challenging, being still in its infancy. Here, we propose a general strategy to design highly entangled high-dimensional spin-orbital single-photon sources by taking full advantage of the spatial freedom to design QE-coupled composite (i.e., Moiré/multipart) metasurfaces. We demonstrate the generation of arbitrary vectorial spin-orbital photon emission in high-dimensional Hilbert spaces, mapping the generated states on hybrid-order Bloch spheres. We further realize single-photon sources of high-dimensional spin-orbital quantum emission and experimentally verify the entanglement of high-dimensional superposition states with high fidelity. We believe that the results obtained facilitate further progress in integrated solutions for the deployment of next-generation high-capacity quantum information technologies.

INTRODUCTION

Polarization states of photons carrying spin-angular momentum (SAM) are restricted to two-dimensional alphabet with canonical right ($|R\rangle$) and left ($|L\rangle$) circular polarization (CP) eigen-states as basis modes, although multiple options can be applied in two-dimensional subspaces (*1*–*3*), which can be represented on a standard Bloch (or Poincaré) sphere (*4*, *5*). The spatial modes of photons carrying orbital angular momentum (OAM), which are associated with an azimuthal phase of the form $\exp(i\ell\phi)$ representing the helical twisting of the phase ℓ times the azimuth (ϕ) (*6*, *7*). In principle, there is an infinite number of spatial modes with this discrete countable basis resulting in an extra quanta of OAM per photon, a feature that provides a higher quantum channel capacity, beyond one bit per photon (*8*, *9*). For classical light, numerous investigations have been conducted to explore all freedom degrees of light, especially, toward high-dimensional structured light (*10*, *11*). One of the most attractive directions for extending the degrees of freedom of classical light is the combination of SAM and OAM, which elevates scalar OAM beams to vector vortex beams and gives rise to spin-orbit vectorial states (*12*, *13*), especially with the help of planar subwavelength artificial structures (i.e., metasurfaces) (*14*–*17*). At the single-photon level, the OAM manipulation was demonstrated only two decades ago (*18*, *19*), with the flexible control of quantum state of light being far less developed in comparison with classical free-space light (*20*–*22*).

Conventional approaches for shaping quantum light inevitably rely on the use of external and bulky optical components, including lens, waveplates, polarizers, spatial light modulators (SLMs), and digital micromirror devices (*23*–*26*). Although optical metasurfaces have been designed to manipulate single-photon beams, in most cases, they are still treated as external components, like their bulky counterparts, which are placed away from the photon sources (*27*–*30*). By integrating quantum emitters (QEs) with nanophotonic structures, such as photonic crystals or microrings (*31*–*34*), the generation of single photons with SAM or OAM was respectively realized though with strict conditions. Another avenue for realizing advanced single-photon sources is to use metasurfaces that are coupled on-chip to QEs and designed to generate well-collimated single-photon beams with relatively high efficiency (*35*–*38*). On-chip generation of single photons encoded with SAM was first realized and then extended to OAM (*35*, *36*). Single mode circularly polarized single-photon vortex beams and linearly polarized single-photon vortex beams have also been realized with QE-coupled anisotropic metasurfaces (*39*, *40*). Recently, the vectoral scattering holography (VSH) approach has been proposed as an inverse design method for creating on-chip nanostructures integrated with QEs (*41*–*43*). In this approach, the reference wave is QE-excited surface plasmon polaritons (SPPs) that radially propagate on the surface, the framework that is different from the traditional holography based on free-space light. The developed VSH approach has been applied to generate both single-channel (*41*) and multichannel (*42*, *43*) photon emission with desired polarizations and off-normal propagation directions. Although the previous works demonstrated the possibility for on-chip generation of SAM and OAM photon states, extending the developed approach to generating high-dimensional structured single photons remains to be challenging and it is still elusive to find a reliable way for designing nanostructures to control the superimposition of spin-orbital photon emission.

In this work, we propose a general approach for designing single-photon sources of high-dimensional spin-orbital photon beams to drastically expand the degrees of freedom in comparison with the state of the art. The principle is to design on-chip QE-coupled composite metasurfaces that would make full use of the spatial freedom and outcouple QE-excited (nonradiative) SPPs into photon emission encoded with vectorial spin-orbital states. We develop the VSH approach to separately generate the interference patterns of spin-orbital waves (i.e., signal waves) and QE-excited SPPs (i.e., reference waves), which are then superimposed as a Moiré pattern and binarized further to be used for fabricating (around a QE) a nanoridge patterned metasurface. The generation of arbitrary vectoral spin-orbital quantum emission in high-dimensional Hilbert spaces is presented with the hybrid-order Bloch spheres (HOBSs), revealing accurate manipulation of arbitrary vectoral spin-orbital

[1]Center for Nano Optics, University of Southern Denmark, DK-5230 Odense M, Denmark. [2]L.F. Vereshchagin Institute for High Pressure Physics, Russian Academy of Sciences, Troitsk, Moscow 142190, Russia. [3]GREMAN, CNRS, UMR 7347, INSA CVL, Université de Tours, 37200 Tours, France.
*Corresponding author. Email: yk@mci.sdu.dk (Y.K.); seib@mci.sdu.dk (S.I.B.)
†These authors contributed equally to this work.

states. Furthermore, using signal waves with different topological charges and beam radii to generate spatially resolved metasurfaces, we realize single-photon sources of high-dimensional spin-orbital quantum emission and experimentally demonstrate the entanglement of high-dimensional superposition states with high fidelity. The proposed approach and the designed single-photon sources facilitate further progress in quantum nanophotonics and open avenues for advanced photonic quantum information technologies.

RESULTS

Operation principle

High-dimensional spin-orbital quantum light sources can be realized by on-chip integration of QEs and composite metasurfaces, which are obtained by calculating, superimposing, and binarizing several interference patterns (Fig. 1). A QE, located atop a silica (SiO2)–covered silver (Ag) film, is considered as a vertical electric dipole that can efficiently excite SPPs radially propagating along the surface. To outcouple the QE-excited nonradiative SPPs into upward-going single-photon emission encoded with high-dimensional states, composite nanostructures should be carefully designed by making full use of spatial freedom of the space including both the azimuthal and the radial directions. The developed VSH approach is a promising way to design QE-coupled nanostructures for the generation of photon emission with desired polarizations and propagation directions (*41*–*43*), while precisely controlling the ratio and phase differences of generated spin-orbital waves is yet to be realized. Here, we extend the VSH approach to the high-dimensional regime exemplifying the case for two signal waves to be reconstructed (note S1 and fig. S1). Two spin-orbital waves (i.e., signal waves, $\mathbf{E}_{s1}$ and $\mathbf{E}_{s2}$) with arbitrary amplitude, polarization, and topological charges can be used to separately interfere with QE-excited SPP waves (i.e., reference waves, $\mathbf{E}_{spp}$), as illustrated in Fig. 1B. Here, we use the signal waves with radial polarization, $\mathbf{E}_{s1} = \cos\left(\frac{\theta}{2}\right) e^{i\varphi/2} LG^0_{\ell_1} |\ell_1\rangle \cdot \begin{bmatrix} \cos\phi \\ \sin\phi \end{bmatrix}$ and $\mathbf{E}_{s2} = \sin\left(\frac{\theta}{2}\right) e^{-i\varphi/2} LG^0_{\ell_2} |\ell_2\rangle \cdot \begin{bmatrix} \cos\phi \\ \sin\phi \end{bmatrix}$, because it (e.g., $\mathbf{E}_{s1}$) can be decomposed into $|L\rangle$ and $|R\rangle$ with the corresponding topological charges of $\ell_{L1} = \ell_1 - 1$ and $\ell_{R1} = \ell_1 + 1$ (note S2). The signal waves are the fundamental Laguerre-Gaussian (LG) beam with $LG^0_{\ell_1} = \sqrt{\frac{2}{\pi \ell_1!}} \cdot \frac{1}{w_1} \cdot \exp\left(-\frac{r^2}{w_1^2}\right) \cdot \left(\sqrt{2}\frac{r}{w_1}\right)^{|\ell_1|} \cdot \exp(i\ell_1\phi)$, where the number of radial nodes is 0, w_1 is the LG beam waist, and the radius vector $r = \sqrt{x^2 + y^2}$ (*44*). It should be noted that, in this work, we extend further the VSH approach by introducing the angular parameters (θ, φ) to precisely manipulate the ratio (related to θ) and relative orientation (related to φ) of the signal waves $\mathbf{E}_{s1}$ and $\mathbf{E}_{s2}$. The QE-excited reference waves are in the form of $\mathbf{E}_{spp} \sim \exp(-ik_{spp} \cdot r) \cdot \begin{bmatrix} \cos\phi \\ \sin\phi \end{bmatrix}$, where $k_{spp} = (2\pi/\lambda)N_{spp}$, with N_{spp} being the effective index of SPPs at the targeted wavelength λ of photon emission from QEs. The obtained interference patterns are then superimposed, resulting in a Moiré pattern when considering the spatially overlapped signal waves (i.e., having the same radii) or two spatially resolved patterns corresponding to the spatially

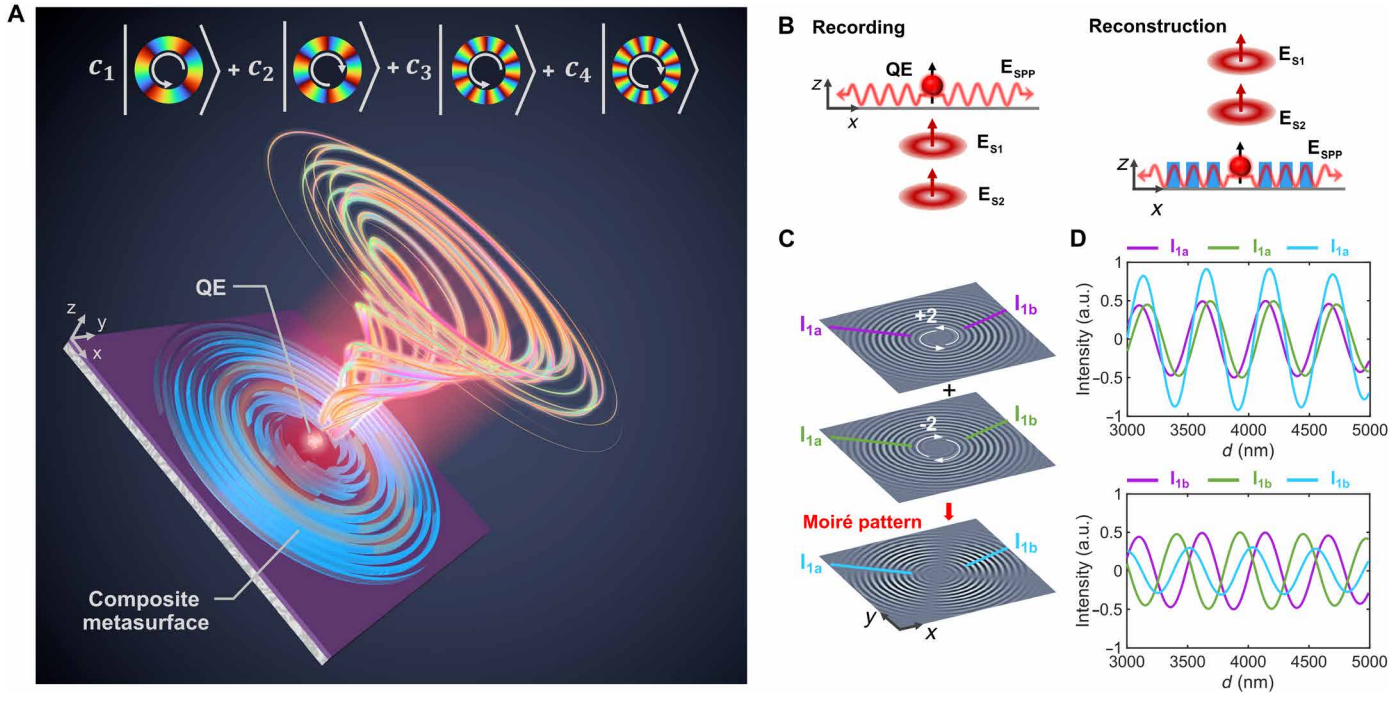

Fig. 1. High-dimensional spin-orbital quantum light sources. (**A**) Direct on-chip generation of high-dimensional spin-orbital quantum light with the QE coupled composite metasurfaces. (**B**) The VSH-based approach for generation of high-dimensional spin-orbital quantum light illustrating the recording and reconstruction process. (**C**) Design of the QE-coupled Moiré metasurface by superimposing two interference patterns of arbitrary spin-orbital signal waves ($\ell_1 = +2$ and $\ell_2 = -2$) and QE-excited SPPs. (**D**) Intensity cross sections of the Moiré interference patterns marked by dashed lines with corresponding colors in (C).

separated (because of different radii) signal waves. Either way, the combined interference pattern is then binarized, into a two-part (conventional) nanoridge pattern or Moiré metasurfaces, as shown in Fig. 1C. For binarizing the interference pattern, the threshold should be properly chosen to make sure the filling ratio χ of the generated metasurfaces corresponds to the SPP effective index used in the design, satisfying the relationship $N_{spp} = (1 - \chi)N_{eff}(\text{air}) + \chi N_{eff}(\text{dieletric})$, where $N_{eff}(\text{air})$ and $N_{eff}(\text{dieletric})$ are the effective mode indices for QE-excited SPP waves propagating in Ag-SiO_2 interface without and with dielectric layer (*35*). The thickness of metasurfaces is set as 150 nm to ensure efficient outcoupling of QE-excited SPPs into free-space photon emission. To show the superposition of two interference patterns into Moiré pattern more clearly, we mark two dashed lines on the patterns 1 and 2 and their superimposed pattern with different colors, displaying the intensity cross sections in Fig. 1D. Because of different intensity distributions of two patterns, which originate from different signal waves used for the interference with the reference SPP field, the intensity of the superimposed Moiré pattern in different areas varies across the metasurface (cf. Fig. 1D, top and bottom). The obtained composite interference pattern and the corresponding Moiré metasurface have more freedom than previous designs, originating not only from the properties of two (or even more) signal waves themselves but also from their intensity ratios and relative orientations (figs. S2 to S4) that can be completely and accurately controlled during the design process (i.e., during the computer-aided recording procedure in the VSH). The same features are also found when superimposing several spatially resolved interference patterns generated with signal waves having spatially separate supports because of different topological charges and beam radii. It is therefore possible to directly (at-source) generate quantum structured light encoded with composite high-dimensional states using either of the regimes described above. This approach represents notable improvement over previous works on generation of single-photon vortex states $|L\rangle|\ell_L\rangle + |R\rangle|\ell_R\rangle$ (*36*) and $|R\rangle|\ell_R\rangle$ (*39*). Moreover, with our VSH-based design strategy, more high-dimensional states can be generated, e.g., $|L\rangle\{|\ell_{L1}\rangle + |\ell_{L2}\rangle + |\ell_{L3}\rangle\cdots\} + |R\rangle\{|\ell_{R1}\rangle + |\ell_{R2}\rangle + |\ell_{R3}\rangle\cdots\}$, simply by introducing more signal waves in the design process.

Arbitrary vectoral spin-orbital quantum emission

First, we consider high-dimensional vectoral spin-orbital beams composed of two CPs, each carrying two different OAMs

$$|\Psi\rangle = \frac{1}{\sqrt{2}}|L\rangle\left\{\cos\left(\frac{\theta}{2}\right)e^{i\varphi/2}|\ell_{L1}\rangle + \sin\left(\frac{\theta}{2}\right)e^{-i\varphi/2}|\ell_{L2}\rangle\right\} + \frac{1}{\sqrt{2}}|R\rangle\left\{\cos\left(\frac{\theta}{2}\right)e^{i\varphi/2}|\ell_{R1}\rangle + \sin\left(\frac{\theta}{2}\right)e^{-i\varphi/2}|\ell_{R2}\rangle\right\} \quad (1)$$

where $|L\rangle = (\mathbf{e}_x + i\mathbf{e}_x)/\sqrt{2}$ and $|R\rangle = (\mathbf{e}_x - i\mathbf{e}_x)/\sqrt{2}$ represent two orthonormal CP states with $\mathbf{e}_x$ and $\mathbf{e}_y$ being the unit vectors along the x and y axes in the Cartesian coordinate system, θ and φ are the constants, and $|\ell_{L1}\rangle$, $|\ell_{L2}\rangle$, $|\ell_{R1}\rangle$, and $|\ell_{R2}\rangle$ represent the OAM states. For example, $|\ell_{L1}\rangle$ is associated with the helical wave front described by the azimuthal phase factor $\exp(i\ell_{L1}\phi)$. The above state (Eq. 1) can be graphically shown using the spherical coordinates (θ, φ) in two HOBSs of orders (ℓ_{L1}, ℓ_{L2}) and (ℓ_{R1}, ℓ_{R2}), respectively. It is easily seen that any arbitrary spin-orbital states described with Eq. 1 can be represented by two points on two HOBSs. For instance, considering the HOBS related to $|L\rangle$ states (Fig. 2A), the north (0, 0) and south (π, 0) poles of the HOBS represent two orthonormal sates of $\frac{1}{\sqrt{2}}|L\rangle|+1\rangle$ and $\frac{1}{\sqrt{2}}|L\rangle|-3\rangle$, which are associated with two left-hand CP (LCP) vortex fields with topological the charges of $\ell_{L1} = +1$ and $\ell_{L2} = -3$, respectively. The HOBS equator corresponds to the hybrid states with equal contributions (i.e., with the same amplitudes) from these two basis states $\left(\text{i.e.,}\frac{1}{\sqrt{2}}|L\rangle|+1\rangle \text{ and } \frac{1}{\sqrt{2}}|L\rangle|-3\rangle\right)$, which can be described as $(e^{i\varphi/2}|L\rangle|+1\rangle + e^{-i\varphi/2}|L\rangle|-3\rangle)/2$. By varying parameters θ and φ, arbitrary vectoral spin-orbital quantum emission can be realized, mapping any position on the HOBS. Similarly, considering the HOBS related to $|R\rangle$ states (Fig. 2A), where the north and south poles are $\frac{1}{\sqrt{2}}|R\rangle|+3\rangle$ and $\frac{1}{\sqrt{2}}|R\rangle|-1\rangle$, the HOBS points represent superpositions of right-hand circularly polarized (RCP) vortex fields with topological charges of $\ell_{R1} = +3$ and $\ell_{R2} = -1$. It should be noted that because of radially polarized SPP waves used as the reference waves, the generated photon emission always contains both $|L\rangle$ and $|R\rangle$ state components. This is due to the reconstructed (with nanoridge metasurfaces) photon emission featuring the same polarization as the reference waves, i.e., the radial polarization, which can be decomposed into LCP and RCP wave components, showing the natural superiority for the direct generation of spin-orbital photon emission by the proposed VSH approach (note S2). In the meantime, the topological charges of LCP and RCP components are strictly related, i.e., $\ell_R - \ell_L = 2$, as they are generated from the radial polarization. This strict relationship can be made redundant by introducing anisotropic scatterers (*39*) to construct holographic metasurfaces.

For the experimental generation composite vectoral spin-orbital quantum emission, we first design the corresponding QE-coupled Moiré metasurfaces using the VSH approach as described above (Fig. 1, B to D). The two interference patterns, calculated for the SPP reference wave interfering with two radially polarized signal waves encoded with two OAMs, +2 and −2, are superimposed as a Moiré pattern, which is then binarized into the Moiré metasurface to be fabricated around QE. We use nanodiamonds containing nitrogen vacancy center (NV-ND) as QEs, whose emission peak appears at around 670 nm. The metasurface, made of hydrogen silsesquioxane (HSQ), is fabricated around a preselected NV-ND. Three metasurfaces with (θ, φ) being set as ($\pi/6$, $\pi/4$), ($\pi/2$, $\pi/4$), and ($2\pi/3$, $\pi/4$), respectively, were fabricated (Fig. 2B), and the corresponding quantum emission was characterized by the combination of a quarter-waveplate and a linear polarizer taking Fourier plane images (see the "Optical characterization" section). The simulated and experimental far-field distributions shown in the insets in Fig. 2A, with the exceptional points being marked, reveal the combination of different topological states and demonstrate good overall correspondence between the simulated and experimental emission patterns [numerical aperture (NA) = 0.5]. For small θ (e.g., $\theta = \pi/6$), the emission is dominated by the nearby pole state $\left(\frac{1}{\sqrt{2}}|L\rangle|+1\rangle \text{for LCP and} \frac{1}{\sqrt{2}}|R\rangle|+3\rangle \text{ for RCP}\right)$. The emission gradually transforms to the opposite pole state $\left(\frac{1}{\sqrt{2}}|L\rangle|-3\rangle \text{ or } \frac{1}{\sqrt{2}}|R\rangle|-1\rangle\right)$ with increasing the azimuthal angle θ. At the HOBS equator with $\theta = \pi/2$ two states contribute equally as described above. Therefore, by changing the angular parameters (θ, φ) of signal waves used in the VSH design procedure, one can actively manipulate high-dimensional states of the generated photon emission (figs. S3 and S4). Furthermore, using simulations of quantum emission from the correspondingly designed QE-coupled Moiré

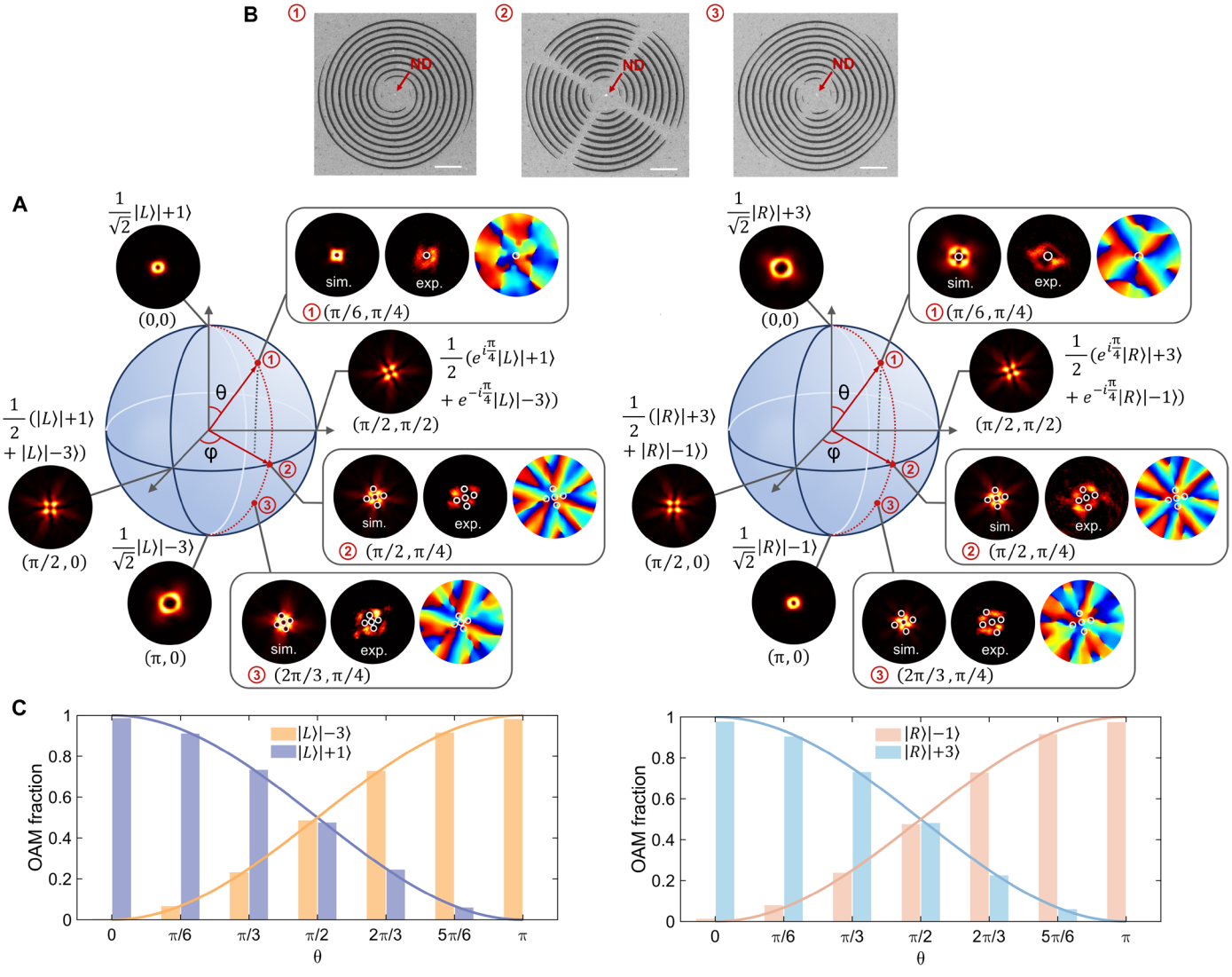

Fig. 2. Generation of arbitrary vectoral spin-orbital quantum emission in high-dimensional Hilbert spaces. (**A**) HOBSs presenting structured photon emission vortex beams with vectoral spin-orbital states, $|L\rangle$ (left) and $|R\rangle$ (right). The insets show the far-field emission intensity patterns (NA = 0.5) and the corresponding phase profiles of three QE-coupled Moiré metasurfaces. The metasurfaces are related to the signal beams with $\ell_1 = +2$ and $\ell_2 = -2$. (**B**) The scanning electron microscope (SEM) images of three QE-coupled Moiré metasurfaces with (θ, φ) being set as (π/6, π/4), (π/2, π/4), and (2π/3, π/4), from the left to the right. Scale bars, 2 μm. (**C**) The modal spectrum changing with the azimuthal angle θ (analytic with lines and simulation with histogram) of $|L\rangle$ (left) and $|R\rangle$ (right).

metasurfaces, we quantified the contributions from differently weighted OAM states, both for LCP and RCP. It is seen (Fig. 2C) that, by varying the azimuthal angle θ in the design process, the fraction of OAM states in the generated photon emission changes according to the analytic (harmonic) dependencies (Eq. 1).

High-dimensional single-photon sources

To demonstrate the use of composite multipart metasurfaces for realizing high-dimensional single-photon sources, we consider the case of two radially polarized signal beams $\mathbf{E}_{s1}$ and $\mathbf{E}_{s2}$ having different topological charges ($\ell_1 = 5$ and $\ell_2 = 11$) and different beam radii ($w_1 = 6.5\lambda$ and $w_2 = 1.5\lambda$), resulting in two spatially resolved (radially separated) interference patterns (Fig. 1A). We further set the HOBS angular parameters (θ, φ) to be (π/2, π/4), ensuring equal contributions to the hybrid state (Eq. 1). In this case, we use nanodiamonds containing single germanium vacancy centers (GeV-NDs) as QEs capable of generating single photons at room temperature with a narrow emission peak at 602 nm. The multipart metasurface is designed with the VSH approach and then fabricated around preselected a GeV-ND (fig. S5). From the scanning electron microscopy (SEM) and atomic force microscopy (AFM) images (Fig. 3A), it is seen that the GeV-ND is located precisely at the center of high-quality fabricated metasurface. A tightly focused radially polarized laser beam (532 nm), which can produce a strong electric field component ($\mathbf{E}_z$) perpendicular to the surface, is applied for preselecting and efficiently exciting the GeV-ND with the sufficiently large normal dipole projection of the QE radiative transition (figs. S6 and S7). For both simulated and experimentally obtained far-field emission patterns, one distinguishes two, inner and outer, parts of the photon emission (Fig. 3B). The inner and outer parts of LCP emission are related to

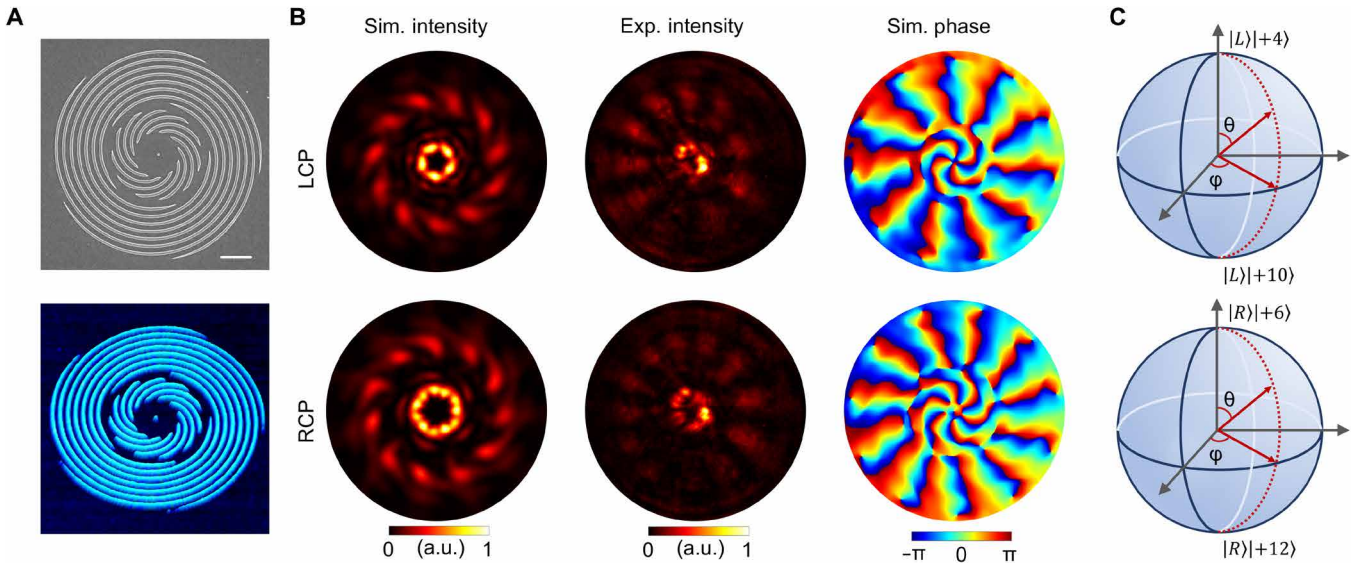

Fig. 3. Generation of composite high-dimensional spin-orbital quantum emission. (**A**) SEM (top) and AFM (bottom) images of the sample. Scale bar, 2 μm. The metasurfaces is related to the signal beams with $\ell_1 = +5$ and $\ell_2 = +11$. (**B**) Simulation and experimental results of the emission patterns (NA = 0.9) and corresponding phase profiles of LCP (top row) and RCP (bottom row) states. (**C**) HOBSs presenting composite photon emission vortex beams in high-dimensional Hilbert spaces of LCP (top row) and RCP (bottom row) states.

the superposition of $|L\rangle|+4\rangle$ and $|L\rangle|+10\rangle$ states, while the inner and outer parts of RCP emission are related to the superposition of $|R\rangle|+6\rangle$ and $|R\rangle|+12\rangle$ states, respectively. These OAM encoded in the LCP and RCP emissions can directly be deduced from the emission phase distributions. With the used design parameters, the generated states are located on the HOBS equators (Fig. 3C). The number of spiral arms (i.e., $m = 5$ and $m = 11$, respectively) of the metasurfaces in two regions equals to the topological charges ($\ell_1 = 5$ and $\ell_2 = 11$) of the two radially polarized signal waves. Therefore, the generated spiral metasurfaces provides external phase distribution for the radially polarized SPP waves, which are outcoupled to photon emission and can be decomposed into $|L\rangle$ and $|R\rangle$ with the topological charges of $m - 1$ and $m + 1$. Similar features can also be found in the previously considered Moiré metasurface, which is composed of two interference patterns exhibiting two double spirals of opposite chirality, i.e., $m = +2$ and $m = -2$ (Fig. 2B).

Entanglement of high-dimensional superposition states

To explicitly validate the entanglement between high-dimensional composite states, we perform the quantum state tomography (QST) to characterize the entangled states of different modes with projection measurements with different combination of polarization and OAM basis (note S3 and tables S1 and S2). In the experiment, we used quarter-waveplate, linear polarizer, and half-waveplate to project the photon emission into different elements of the polarization basis and an SLM to project the photon emission into different OAM basis element (fig. S7). We define $|\Psi_a\rangle = |R\rangle|+6\rangle + |R\rangle|+12\rangle$, $|\Psi_b\rangle = |R\rangle|+4\rangle + |R\rangle|+10\rangle$, $|\Psi_c\rangle = |L\rangle|+6\rangle + |L\rangle|+12\rangle$, and $|\Psi_d\rangle = |L\rangle|+4\rangle + |L\rangle|+10\rangle$. The density matrices for $|\Psi_1\rangle = \frac{1}{\sqrt{2}}\left(|L\rangle|\ell_L = +4\rangle + |R\rangle|\ell_R = +6\rangle\right)$ and $|\Psi_2\rangle = \frac{1}{\sqrt{2}}\left(|L\rangle|\ell_L = +10\rangle + |R\rangle|\ell_R = +12\rangle\right)$ are separately characterized with twice 16-projection measurements to recover the density matrices (figs. S8 and S9). It can be seen from the density matrices that it is an entangled high-dimensional states (Fig. 4, A and B). The concurrences obtained from the simulation and experimental results are 0.95 and 0.88, respectively, demonstrating that the high-dimensional superposition states of different modes are highly entangled. The fidelity between the reconstructed density matrices of the predicted and experimentally obtained states is defined as $F(\rho_t, \rho_{exp}) = \left[\mathrm{Tr}\left(\sqrt{\sqrt{\rho_t}\rho_{exp}\sqrt{\rho_t}}\right)\right]^2$, where ρ_t and ρ_{exp} are the density matrices of the entangled state of predicted results and the measured results, respectively. The fidelity between the simulated and experimentally measured states is 0.89, which proves that the experimentally obtained quantum state is close to the simulation. The reasons for nonunity fidelity may rise from the nanofabrication error and the deterioration of relatively weak single-photon emission during passing through number of optical components in experimental measurements. We further analyze the robustness of the design by shifting the QE location over 50 nm in both x and y directions, as well as by applying blue and red wavelength shifts (±5 nm, i.e., to 597 and 607 nm). We found that the generated states maintain high fidelities (>0.95) compared to the ideal case (fig. S10). The high fidelities and robustness demonstrate the potential of using QE-coupled composite metasurfaces for high-dimensional quantum emission, with special attention to be paid to the proper orientation of QE radiative transition. The emission spectra of the GeV-ND before and after the QE coupling to the metasurface are practically identical, except for some intensity enhancement (Fig. 4C), showing narrow-band fluorescence emission peaks around 602 nm, where the counts increase may attribute to the Purcell enhancement and enhanced collection after coupling with metasurface. The second-order correlation functions are measured by Hanbury Brown-Twiss setup (fig. S6), showing $g^{(2)}(0) = 0.11$ and 0.21 before and after coupling with metasurface, respectively (Fig. 4D), indicating excellent and stable single-photon properties at room temperature. The single-photon performance might be improved by using low-fluorescence materials to construct metasurfaces and conducting the experiment at cryogenic temperatures.

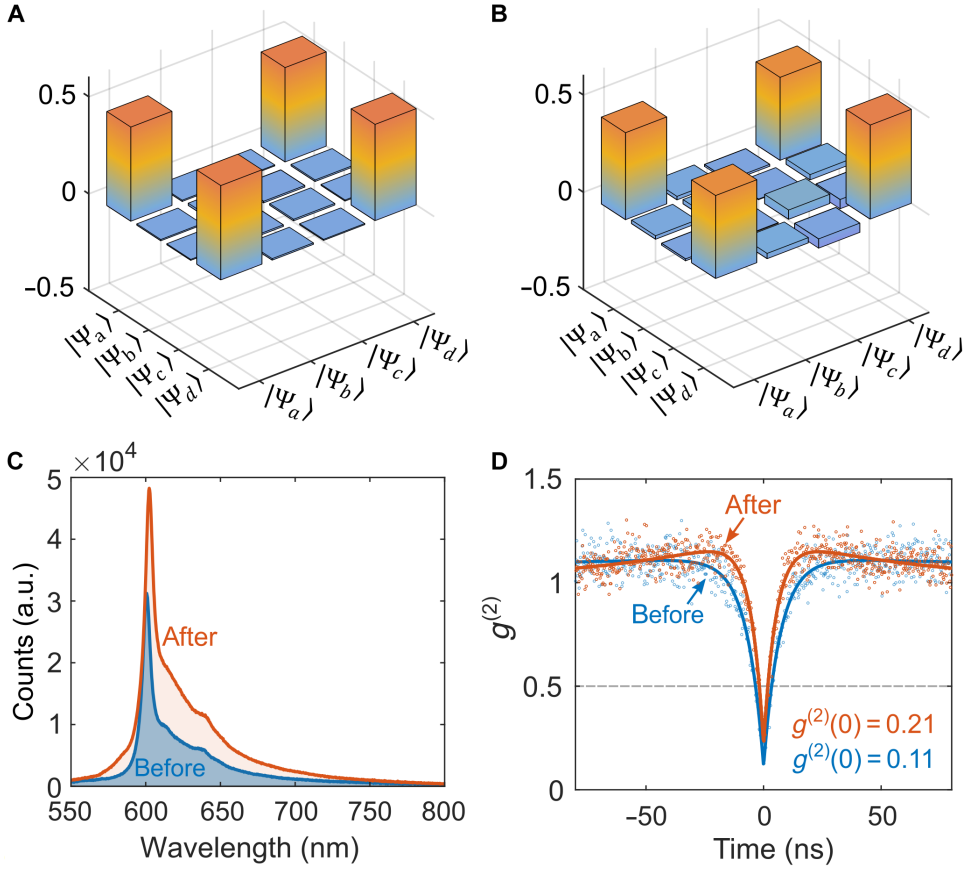

Fig. 4. Demonstration of entanglement of single-photon emission with composite high-dimensional superposition states. (**A**) The simulated density matrices density matrix for the entangled state. (**B**) The experimentally measured density matrix recovered for the entangled state by using QST. (**C**) Spectrum and (**D**) autocorrelation comparison of QE before and after coupling with metasurfaces.

DISCUSSION

In the preceding, we have proposed a general strategy for designing high-dimensional spin-orbital single-photon sources based on QE-coupled composite (i.e., Moiré/multipart) metasurfaces, getting rid of external components like bulky optical components or metalens (*19*, *45*). In comparison with recently reported Moiré metasurfaces for shaping classical free-space light (*46*, *47*), here, we combine the holography approach and Moiré pattern to on-chip generate quantum light states by taking full advantage of the spatial degrees of freedom in designing metasurface patterns obtained from the interference of spin-orbital waves and QE-excited SPPs. We have demonstrated the generation of arbitrary vectorial spin-orbital photon emission in high-dimensional Hilbert spaces, which is represented with the HOBSs, showing the capability of precise manipulation of high-dimensional states by controlling the weighting parameters signal waves in the designing process. This can be viewed as an inverse design approach to generate composite OAM modes, which is entirely different strategy from that used the angular gratings to design the spin-orbital microlaser (*13*, *48*) and optical vortex microcombs (*49*, *50*).

Moreover, our approach can be extended to design more high-dimensional quantum light sources by increasing the number of signal waves to generate interference patterns or separating the in-plane area to several parts, allowing for arbitrary generation of high-dimensional superposition states. By using two signal waves with different topological charges and beam sizes to generate the two-part composite metasurface, we realize the single-photon source of high-dimensional spin-orbital quantum emission. We think that it is definitely possible to generate the quantum states using different radial and azimuthal degrees of freedom and keeping the same beam size parameter, but working out the general implementation approach for their arbitrary combination is challenging and goes beyond the design approach presented in this work. It may also be possible to realize on-chip single-photon skyrmion sources, featuring more complex vectorial field structures with versatile and resilient topological characteristics (*51*, *52*). Furthermore, we characterize the entangled LCP and RCP superposition states, revealing the entanglement of single-photon emission with composite high-dimensional superposition states with the high fidelity. Last, it is important to note that design strategy is general and can be used for other QEs with different wavelengths (*53*, *54*), e.g., with those single-photon emitters operated at cryogenic temperatures, the performance may be further improved. We believe that the proposed approach and the designed single-photon sources facilitate further progress in integrated solutions for the deployment of next-generation high-capacity quantum information processing technologies (*11*, *55*, *56*).

MATERIALS AND METHODS

Numerical simulations

Numerical simulations of QE-coupled metasurfaces were performed with three-dimensional finite-difference time-domain method. The QE was simulated as a *z*-direction electric dipole radiating at 602 nm, fitting the emission peak of GeV-ND. The dipole was placed 50 nm atop the SiO_2 spacer (20 nm) and silver film (150 nm) and in the center of dielectric nanostructures (with thickness of 150 nm and refractive index of 1.41). A two-dimensional monitor 150 nm atop the configuration was employed to collect far-filed electric field by near- to far-field transformation method.

Device fabrication

Fabrication of QE-coupled metasurfaces followed a well-established sequence of technological steps (fig. S5). A 150-nm-thick silver film was first deposited on the silicon substrate by the thermal evaporation, followed by a 20-nm-thick SiO_2 layer being deposited by the magnetron sputtering method. Then, a group of gold markers were fabricated on the substrate by a combined process of EBL (JEOL-6490 system; accelerating voltage, 30 kV), gold deposition, and lift-off. Subsequently, solution of GeV-NDs was spin-coated with proper diluted concentration. After preselecting GeV-NDs by the fluorescence scan and characterizing quantum properties, the positions of candidates are determined by the dark-field microscope image with the precise alignment procedure, in which we use prefabricated markers to build (*x*, *y*) coordinate system in the surface plane and then determine the coordinates of a suitable ND by fitting two Gaussian distributions to the diffraction-limited spot of the ND (*35*, *36*). A negative photoresist (HSQ) was subsequently spin-coated at 3000 rpm, for 45 s, and heated at the hotplate on 160°C for 2 min to form a ~150-nm layer, which was examined by the AFM (NT-MDT NTEGRA). According to the relative positions of NDs, the metasurface configurations obtained from the VSH approach were written using a properly adjusted electron-beam dose. Subsequently, a second round EBL was then carried out on the resist around GeV-NDs to fabricate the designed metasurfaces. Last, QE-coupled metasurfaces were obtained by development with the tetramethylammonium hydroxide solution (for 4 min) and water (for 60 s).

Optical characterization

The QE-coupled metasurfaces was characterized with the experimental setup as shown in figs. S6 and S7. Radially polarized 532-nm laser beam was used to drive and preselect GeV-NDs that can form a dominant dipole moment perpendicular to the substrate surface. The excitation and collection of photon emission were by the same objective with NA = 0.9 (The Olympus MPLFLN ×100). Fluorescence imaging was performed by a synchronous movement of piezo-stage with mounted sample and projecting the collected fluorescence emission to the avalanche photo diodes (APDs). Fluorescence spectra were measured using the spectrometer (Andor Ultra 888 USB3-BV) operating within 540 to 820 nm. Second-order correlation was recorded by registering the temporal delay between photon detection events between APD1 and APD2 in a start-stop configuration, using an electronic timing box (Picharp-300; Pico quant). The LCP and RCP emission patterns were measured by the combination of a quarter-waveplate and a linear polarizer taking Fourier plane images. An SLM was used to generate the computed holograms with different topological charges. The reflected light from the incident light was filtered out by a set of dichroic mirrors (Semrock FF535-SDi01/FF552-Di02) and with a long-pass filter 550 nm (Thorlabs FELH0550) and a band-pass filter 605 ± 8 nm. The quantum state topography was performed based on the polarization and OAM coincidence with a set of superpositions of polarization and OAM basis (note S3 and fig. S8 and S9).

Supplementary Materials

This PDF file includes:

Supplementary Text
Figs. S1 to S10
Tables S1 and S2
References

REFERENCES AND NOTES

1. P. G. Kwiat, K. Mattle, H. Weinfurter, A. Zeilinger, A. V. Sergienko, Y. Shih, New high-intensity source of polarization-entangled photon pairs. *Phys. Rev. Lett.* **75**, 4337–4341 (1995).
2. D. Bouwmeester, J. W. Pan, K. Mattle, M. Eibl, H. Weinfurter, A. Zeilinger, Experimental quantum teleportation. *Nature* **390**, 575–579 (1997).
3. J. Ni, C. Huang, L. M. Zhou, M. Gu, Q. Song, Y. Kivshar, C. W. Qiu, Multidimensional phase singularities in nanophotonics. *Science* **374**, eabj0039 (2021).
4. G. Milione, H. I. Sztul, D. A. Nolan, R. R. Alfano, Higher-order poincaré sphere, Stokes parameters, and the angular momentum of light. *Phys. Rev. Lett.* **107**, 053601 (2011).
5. M. Born, E. Wolf, *Principles of Optics: Electromagnetic Theory of Propagation, Interference and Diffraction of Light* (Elsevier, 2013).
6. S. Franke-Arnold, 30 years of orbital angular momentum of light. *Nat. Rev. Phys.* **4**, 361 (2022).
7. A. Forbes, S. Ramachandran, Q. Zhan, Photonic angular momentum: Progress and perspectives. *Nanophotonics* **11**, 625–631 (2022).
8. M. Erhard, R. Fickler, M. Krenn, A. Zeilinger, Twisted photons: New quantum perspectives in high dimensions. *Light Sci. Appl.* **7**, 17146–1–11 (2018).
9. D. Cozzolino, B. Da Lio, D. Bacco, L. K. Oxenløwe, High-dimensional quantum communication: Benefits, progress, and future challenges. *Adv. Quantum Technol.* **2**, 1900038 (2019).
10. A. Forbes, M. Oliveira, M. Dennis, Structured light. *Nat. Photon.* **15**, 253–262 (2021).
11. C. He, Y. Shen, A. Forbes, Towards higher-dimensional structured light. *Light Sci. Appl.* **11**, 205 (2022).
12. Z. Ji, W. Liu, S. Krylyuk, X. Fan, Z. Zhang, A. Pan, L. Feng, A. Davydov, R. Agarwal, Photocurrent detection of the orbital angular momentum of light. *Science* **368**, 763–767 (2020).
13. Z. Zhang, H. Zhao, S. Wu, T. Wu, X. Qiao, Z. Gao, R. Agarwal, S. Longhi, N. M. Litchinitser, L. Ge, L. Feng, Spin–orbit microlaser emitting in a four-dimensional Hilbert space. *Nature* **612**, 246–251 (2022).
14. R. C. Devlin, A. Ambrosio, N. A. Rubin, J. P. B. Mueller, F. Capasso, Arbitrary spin-to-orbital angular momentum conversion of light. *Science* **358**, 896–901 (2017).
15. H. Sroor, Y. W. Huang, B. Sephton, D. Naidoo, A. Vallés, V. Ginis, C. W. Qiu, A. Ambrosio, F. Capasso, A. Forbes, High-purity orbital angular momentum states from a visible metasurface laser. *Nat. Photon.* **14**, 498–503 (2020).
16. Y. Bao, J. Ni, C. W. Qiu, A minimalist single-layer metasurface for arbitrary and full control of vector vortex beams. *Adv. Mater.* **32**, e1905659 (2020).
17. Y. Ming, Y. Intaravanne, H. Ahmed, M. Kenney, Y. Q. Lu, X. Chen, Creating composite vortex beams with a single geometric metasurface. *Adv. Mater.* **34**, 2109714 (2022).
18. A. Mair, A. Vaziri, G. Weihs, A. Zeilinger, Entanglement of the orbital angular momentum states of photons. *Nature* **412**, 313–316 (2001).
19. I. Nape, B. Sephton, P. Ornelas, C. Moodley, A. Forbes, Quantum structured light in high dimensions. *APL Photon.* **8**, 051101 (2023).
20. A. S. Solntsev, G. S. Agarwal, Y. S. Kivshar, Metasurfaces for quantum photonics. *Nat. Photon.* **15**, 327–336 (2021).
21. Y. Kan, S. I. Bozhevolnyi, Advances in metaphotonics empowered single photon emission. *Adv. Opt. Mater.* **11**, 2202759 (2023).
22. L. Li, Z. Liu, X. Ren, S. Wang, V. C. Su, M. K. Chen, C. H. Chu, H. Y. Kuo, B. Liu, W. Zang, G. Guo, L. Zhang, Z. Wang, S. Zhu, D. P. Tsai, Metalens-array–based high-dimensional and multiphoton quantum source. *Science* **368**, 1487–1490 (2020).
23. X. L. Wang, X. D. Cai, Z. E. Su, M. C. Chen, D. Wu, L. Li, N. L. Liu, C. Y. Lu, J. W. Pan, Quantum teleportation of multiple degrees of freedom of a single photon. *Nature* **518**, 516–519 (2015).
24. Y. Zhang, F. S. Roux, T. Konrad, M. Agnew, J. Leach, A. Forbes, Engineering two-photon high-dimensional states through quantum interference. *Sci. Adv.* **2**, e1501165 (2016).
25. A. Forbes, I. Nape, Quantum mechanics with patterns of light: Progress in high dimensional and multidimensional entanglement with structured light. *AVS Quantum Sci.* **1**, 011701 (2019).

26. A. Anwar, N. Lal, S. Prabhakar, R. P. Singh, Selective tuning of Hilbert spaces in states encoded with spatial modes of light. *New J. Phys.* **22**, 113020 (2020).
27. T. Stav, A. Faerman, E. Maguid, D. Oren, V. Kleiner, E. Hasman, M. Segev, Quantum entanglement of the spin and orbital angular momentum of photons using metamaterials. *Science* **361**, 1101–1104 (2018).
28. K. Wang, J. G. Titchener, S. S. Kruk, L. Xu, H. P. Chung, M. Parry, I. I. Kravchenko, Y. H. Chen, A. S. Solntsev, Y. S. Kivshar, D. N. Neshev, A. A. Sukhorukov, Quantum metasurface for multiphoton interference and state reconstruction. *Science* **361**, 1104–1108 (2018).
29. T.-Y. Huang, R. R. Grote, S. A. Mann, D. A. Hopper, A. L. Exarhos, G. G. Lopez, G. R. Kaighn, E. C. Garnett, L. C. Bassett, A monolithic immersion metalens for imaging solid-state quantum emitters. *Nat. Commun.* **10**, 2392 (2019).
30. H. Ren, S. A. Maier, Nanophotonic materials for twisted-light manipulation. *Adv. Mater.* **35**, 2106692 (2021).
31. I. Söllner, S. Mahmoodian, S. L. Hansen, L. Midolo, A. Javadi, G. Kiršanskė, T. Pregnolato, H. El-Ella, E. H. Lee, J. D. Song, S. Stobbe, P. Lodahl, Deterministic photon–emitter coupling in chiral photonic circuits. *Nat. Nanotechnol.* **10**, 775–778 (2015).
32. B. Chen, Y. Wei, T. Zhao, S. Liu, R. Su, B. Yao, Y. Yu, J. Liu, X. Wang, Bright solid-state sources for single photons with orbital angular momentum. *Nat. Nanotechnol.* **16**, 302–307 (2021).
33. Y. Ma, H. Zhao, N. Liu, Z. Gao, S. S. Mohajerani, L. Xiao, J. Hone, L. Feng, S. Strauf, On-chip spin-orbit locking of quantum emitters in 2D materials for chiral emission. *Optica* **9**, 953 (2022).
34. H. Zhao, Y. Ma, Z. Gao, N. Liu, T. Wu, S. Wu, X. Feng, J. Hone, S. Strauf, L. Feng, High-purity generation and switching of twisted single photons. *Phys. Rev. Lett.* **131**, 183801 (2023).
35. Y. Kan, S. K. H. Andersen, F. Ding, S. Kumar, C. Zhao, S. I. Bozhevolnyi, Metasurface-enabled generation of circularly polarized single photons. *Adv. Mater.* **32**, e1907832 (2020).
36. C. Wu, S. Kumar, Y. Kan, D. Komisar, Z. Wang, S. I. Bozhevolnyi, F. Ding, Room-temperature on-chip orbital angular momentum single-photon sources. *Sci. Adv.* **8**, eabk3075 (2022).
37. Y. Kan, F. Ding, C. Zhao, S. I. Bozhevolnyi, Directional off-normal photon streaming from hybrid plasmon-emitter coupled metasurfaces. *ACS Photonics* **7**, 1111–1116 (2020).
38. D. Komisar, S. Kumar, Y. Kan, C. Wu, S. I. Bozhevolnyi, Generation of radially polarized single photons with plasmonic bullseye antennas. *ACS Photonics* **8**, 2190–2196 (2021).
39. X. Liu, Y. Kan, S. Kumar, D. Komisar, C. Zhao, S. I. Bozhevolnyi, On-chip generation of single-photon circularly polarized single-mode vortex beams. *Sci. Adv.* **9**, eadh0725 (2023).
40. X. Liu, Y. Kan, S. Kumar, L. F. Kulikova, V. A. Davydov, V. N. Agafonov, C. Zhao, S. I. Bozhevolnyi, Ultracompact single-photon sources of linearly polarized vortex beams. *Adv. Mater.* **36**, 2304495 (2024).
41. Y. Kan, S. I. Bozhevolnyi, Molding photon emission with hybrid plasmon-emitter coupled metasurfaces. *Adv. Opt. Mater.* **10**, 2102697 (2022).
42. D. Komisar, S. Kumar, Y. Kan, C. Meng, L. F. Kulikova, V. A. Davydov, V. N. Agafonov, S. I. Bozhevolnyi, Multiple channelling single-photon emission with scattering holography designed metasurfaces. *Nat. Commun.* **14**, 6253 (2023).
43. Y. Kan, X. Liu, S. Kumar, S. I. Bozhevolnyi, Multichannel quantum emission with on-chip emitter-coupled holographic metasurfaces. *ACS Nano* **17**, 20308–20314 (2023).
44. E. Abramochkin, V. Volostnikov, Generalized Gaussian beams. *J. Opt.* **6**, S157–S161 (2004).
45. J. Ma, J. Zhang, J. Horder, A. A. Sukhorukov, M. Toth, D. N. Neshev, I. Aharonovich, Engineering quantum light sources with flat optics. *Adv. Mater.* **36**, 2313589 (2024).
46. S. Liu, S. Ma, R. Shao, L. Zhang, T. Yan, Q. Ma, S. Zhang, T. J. Cui, Moiré metasurfaces for dynamic beamforming. *Sci. Adv.* **8**, eabo1511 (2022).
47. Z. Wu, Y. Zheng, Moiré metamaterials and metasurfaces. *Adv. Opt. Mater.* **6**, 1701057 (2018).
48. Z. Zhang, X. Qiao, B. Midya, K. Liu, J. Sun, T. Wu, W. Liu, R. Agarwal, J. M. Jornet, S. Longhi, N. M. Litchinitser, L. Feng, Tunable topological charge vortex microlaser. *Science* **368**, 760–763 (2020).
49. B. Chen, Y. Zhou, Y. Liu, C. Ye, Q. Cao, P. Huang, C. Kim, Y. Zheng, L. K. Oxenløwe, K. Yvind, J. Li, J. Li, Y. Zhang, C. Dong, S. Fu, Q. Zhan, X. Wang, M. Pu, J. Liu, Integrated optical vortex microcomb. *Nat. Photon.* **18**, 625–631 (2024).
50. Y. Liu, C. Lao, M. Wang, Y. Cheng, Y. Wang, S. Fu, C. Gao, J. Wang, B.-B. Li, Q. Gong, Y.-F. Xiao, W. Liu, Q.-F. Yang, Integrated vortex soliton microcombs. *Nat. Photon.* **18**, 632–637 (2024).
51. Y. Shen, Q. Zhang, P. Shi, L. Du, X. Yuan, A. V. Zayats, Optical skyrmions and other topological quasiparticles of light. *Nat. Photon.* **18**, 15–25 (2024).
52. P. Ornelas, I. Nape, R. de Mello Koch, A. Forbes, Non-local skyrmions as topologically resilient quantum entangled states of light. *Nat. Photon.* **18**, 258–266 (2024).
53. I. Aharonovich, D. Englund, M. Toth, Solid-state single-photon emitters. *Nat. Photonics* **10**, 631–641 (2016).
54. P. Senellart, G. Solomon, A. White, High-performance semiconductor quantum-dot single-photon sources. *Nat. Nanotechnol.* **12**, 1026–1039 (2017).
55. J. Wang, S. Paesani, Y. Ding, R. Santagati, P. Skrzypczyk, A. Salavrakos, J. Tura, R. Augusiak, L. Mančinska, D. Bacco, D. Bonneau, J. W. Silverstone, Q. Gong, A. Acín, K. Rottwitt, L. K. Oxenløwe, J. L. O'Brien, A. Laing, M. G. Thompson, Multidimensional quantum entanglement with large-scale integrated optics. *Science* **360**, 285–291 (2018).
56. M. Pompili, S. L. N. Hermans, S. Baier, H. K. C. Beukers, P. C. Humphreys, R. N. Schouten, R. F. L. Vermeulen, M. J. Tiggelman, L. Dos Santos Martins, B. Dirkse, S. Wehner, R. Hanson, Realization of a multinode quantum network of remote solid-state qubits. *Science* **372**, 259–264 (2021).
57. P.Hariharan, *Optical Holography* (Cambridge Univ. Press, 2012).
58. E. Toninelli, B. Ndagano, A. Vallés, B. Sephton, I. Nape, A. Ambrosio, F. Capasso, M. J. Padgett, A. Forbes, Concepts in quantum state tomography and classical implementation with intense light: A tutorial. *Adv. Opt. Photon.* **11**, 67–134 (2019).
59. P. K. Jha, X. Ni, C. Wu, Y. Wang, X. Zhang, Metasurface-enabled remote quantum interference. *Phys. Rev. Lett.* **115**, 025501 (2015).

Acknowledgments: X.L. acknowledges the award for outstanding Ph.D. graduates of Shanghai Jiao Tong University. **Funding:** This work was supported by the National Natural Science Foundation of China grant 62105150 (Y.K.), European Union's Horizon Europe research and innovation program under the Marie Skłodowska-Curie Action grant 101064471 (Y.K.), Natural Science Foundation of Jiangsu Province grant BK20210289 (Y.K.), and Villum Kann Rasmussen Foundation (Award in Technical and Natural Sciences 2019) (S.I.B.). **Author contributions:** Y.K. and S.I.B. conceived the idea. Y.K. performed theoretical modelling. Y.K. and X.L. fabricated samples. Y.K. and X.L. performed experimental measurement. L.F.K., V.A.D., and V.N.A. synthesized the GeV nanodiamonds. Y.K., X.L., S.K., and S.I.B. analyzed the data. S.I.B. and Y.K. supervised the project. Y.H.K. wrote the manuscript, with contributions from all authors. **Competing interests:** The authors declare that they have no competing interests. **Data and materials availability:** All data needed to evaluate the conclusions in the paper are present in the paper and/or the Supplementary Materials.

Submitted 23 May 2024
Accepted 4 October 2024
Published 6 November 2024
10.1126/sciadv.adq6298